Forward J/ψ production in U + U collisions at √sN N = 193 GeV

(PHENIX Collaboration) Adare, A.; ...; Makek, Mihael; ...; Zou, L.

Source / Izvornik: **Physical Review C, 2016, 93**

Journal article, Published version
Rad u časopisu, Objavljena verzija rada (izdavačev PDF)

https://doi.org/10.1103/PhysRevC.93.034903

Forward J/ψ production in U + U collisions at $\sqrt{s_{NN}} = 193$ GeV

A. Adare,[13] C. Aidala,[38,42] N. N. Ajitanand,[60] Y. Akiba,[55,56] R. Akimoto,[12] J. Alexander,[60] M. Alfred,[22] K. Aoki,[31,55]
N. Apadula,[27,61] H. Asano,[34,55] E. T. Atomssa,[61] T. C. Awes,[51] B. Azmoun,[7] V. Babintsev,[23] M. Bai,[6] X. Bai,[11] N. S. Bandara,[41]
B. Bannier,[61] K. N. Barish,[8] S. Bathe,[5,56] V. Baublis,[54] C. Baumann,[7] S. Baumgart,[55] A. Bazilevsky,[7] M. Beaumier,[8]
S. Beckman,[13] R. Belmont,[13,42,65] A. Berdnikov,[58] Y. Berdnikov,[58] D. Black,[8] D. S. Blau,[33] J. S. Bok,[49] K. Boyle,[56]
M. L. Brooks,[38] J. Bryslawskyj,[5] H. Buesching,[7] V. Bumazhnov,[23] S. Butsyk,[48] S. Campbell,[14,27] C.-H. Chen,[56] C. Y. Chi,[14]
M. Chiu,[7] I. J. Choi,[24] J. B. Choi,[10] S. Choi,[59] P. Christiansen,[39] T. Chujo,[64] V. Cianciolo,[51] Z. Citron,[66] B. A. Cole,[14]
N. Cronin,[43,61] N. Crossette,[43] M. Csanád,[16] T. Csörgő,[67] T. W. Danley,[50] A. Datta,[48] M. S. Daugherity,[1] G. David,[7]
K. DeBlasio,[48] K. Dehmelt,[61] A. Denisov,[23] A. Deshpande,[56,61] E. J. Desmond,[7] L. Ding,[27] A. Dion,[61] P. B. Diss,[40] J. H. Do,[68]
L. D'Orazio,[40] O. Drapier,[35] A. Drees,[61] K. A. Drees,[6] J. M. Durham,[38] A. Durum,[23] T. Engelmore,[14] A. Enokizono,[55,57]
S. Esumi,[64] K. O. Eyser,[7] B. Fadem,[43] N. Feege,[61] D. E. Fields,[48] M. Finger,[9] M. Finger, Jr.,[9] F. Fleuret,[35] S. L. Fokin,[33]
J. E. Frantz,[50] A. Franz,[7] A. D. Frawley,[18] Y. Fukao,[31] T. Fusayasu,[45] K. Gainey,[1] C. Gal,[61] P. Gallus,[15] P. Garg,[3]
A. Garishvili,[62] I. Garishvili,[37] H. Ge,[61] F. Giordano,[24] A. Glenn,[37] X. Gong,[60] M. Gonin,[35] Y. Goto,[55,56] R. Granier de
Cassagnac,[35] N. Grau,[2] S. V. Greene,[65] M. Grosse Perdekamp,[24] Y. Gu,[60] T. Gunji,[12] H. Guragain,[19] T. Hachiya,[55]
J. S. Haggerty,[7] K. I. Hahn,[17] H. Hamagaki,[12] H. F. Hamilton,[1] S. Y. Han,[17] J. Hanks,[61] S. Hasegawa,[28] T. O. S. Haseler,[19]
K. Hashimoto,[55,57] R. Hayano,[12] X. He,[19] T. K. Hemmick,[61] T. Hester,[8] J. C. Hill,[27] R. S. Hollis,[8] K. Homma,[21] B. Hong,[32]
T. Hoshino,[21] N. Hotvedt,[27] J. Huang,[7,38] S. Huang,[65] T. Ichihara,[55,56] Y. Ikeda,[55] K. Imai,[28] Y. Imazu,[55] M. Inaba,[64]
A. Iordanova,[8] D. Isenhower,[1] A. Isinhue,[43] D. Ivanishchev,[54] B. V. Jacak,[61] S. J. Jeon,[44] M. Jezghani,[19] J. Jia,[7,60] X. Jiang,[38]
B. M. Johnson,[7] K. S. Joo,[44] D. Jouan,[52] D. S. Jumper,[24] J. Kamin,[61] S. Kanda,[12,31] B. H. Kang,[20] J. H. Kang,[68] J. S. Kang,[20]
J. Kapustinsky,[38] D. Kawall,[41] A. V. Kazantsev,[33] J. A. Key,[48] V. Khachatryan,[61] P. K. Khandai,[3] A. Khanzadeev,[54]
K. M. Kijima,[21] C. Kim,[32] D. J. Kim,[29] E.-J. Kim,[10] G. W. Kim,[17] M. Kim,[59] Y.-J. Kim,[24] Y. K. Kim,[20] B. Kimelman,[43]
E. Kistenev,[7] R. Kitamura,[12] J. Klatsky,[18] D. Kleinjan,[8] P. Kline,[61] T. Koblesky,[13] M. Kofarago,[16] B. Komkov,[54] J. Koster,[56]
D. Kotchetkov,[50] D. Kotov,[54,58] F. Krizek,[29] K. Kurita,[57] M. Kurosawa,[55,56] Y. Kwon,[68] R. Lacey,[60] Y. S. Lai,[14] J. G. Lajoie,[27]
A. Lebedev,[27] D. M. Lee,[38] G. H. Lee,[10] J. Lee,[17] K. B. Lee,[38] K. S. Lee,[32] S. Lee,[68] S. H. Lee,[61] M. J. Leitch,[38] M. Leitgab,[24]
B. Lewis,[61] X. Li,[11] S. H. Lim,[68] M. X. Liu,[38] D. Lynch,[7] C. F. Maguire,[65] Y. I. Makdisi,[6] M. Makek,[66,69] A. Manion,[61]
V. I. Manko,[33] E. Mannel,[7] T. Maruyama,[28] M. McCumber,[13,38] P. L. McGaughey,[38] D. McGlinchey,[13,18] C. McKinney,[24]
A. Meles,[49] M. Mendoza,[8] B. Meredith,[24] Y. Miake,[64] T. Mibe,[31] A. C. Mignerey,[40] A. Milov,[66] D. K. Mishra,[4] J. T. Mitchell,[7]
S. Miyasaka,[55,63] S. Mizuno,[55,64] A. K. Mohanty,[4] S. Mohapatra,[60] P. Montuenga,[24] T. Moon,[68] D. P. Morrison,[7,*]
M. Moskowitz,[43] T. V. Moukhanova,[33] T. Murakami,[34,55] J. Murata,[55,57] A. Mwai,[60] T. Nagae,[34] S. Nagamiya,[31,55]
K. Nagashima,[21] J. L. Nagle,[13,†] M. I. Nagy,[16] I. Nakagawa,[55,56] H. Nakagomi,[55,64] Y. Nakamiya,[21] K. R. Nakamura,[34,55]
T. Nakamura,[55] K. Nakano,[55,63] C. Nattrass,[62] P. K. Netrakanti,[4] M. Nihashi,[21,55] T. Niida,[64] S. Nishimura,[12] R. Nouicer,[7,56]
T. Novák,[30,67] N. Novitzky,[29,61] A. S. Nyanin,[33] E. O'Brien,[7] C. A. Ogilvie,[27] H. Oide,[12] K. Okada,[56] J. D. Orjuela Koop,[13]
J. D. Osborn,[42] A. Oskarsson,[39] K. Ozawa,[31] R. Pak,[7] V. Pantuev,[25] V. Papavassiliou,[49] I. H. Park,[17] J. S. Park,[59] S. Park,[59]
S. K. Park,[32] S. F. Pate,[49] L. Patel,[19] M. Patel,[27] J.-C. Peng,[24] D. V. Perepelitsa,[7,14] G. D. N. Perera,[49] D. Yu. Peressounko,[33]
J. Perry,[27] R. Petti,[7,61] C. Pinkenburg,[7] R. Pinson,[1] R. P. Pisani,[7] M. L. Purschke,[7] H. Qu,[1] J. Rak,[29] B. J. Ramson,[42]
I. Ravinovich,[66] K. F. Read,[51,62] D. Reynolds,[60] V. Riabov,[47,54] Y. Riabov,[54,58] E. Richardson,[40] T. Rinn,[27] N. Riveli,[50]
D. Roach,[65] S. D. Rolnick,[8] M. Rosati,[27] Z. Rowan,[5] J. G. Rubin,[42] M. S. Ryu,[20] B. Sahlmueller,[61] N. Saito,[31] T. Sakaguchi,[7]
H. Sako,[28] V. Samsonov,[47,54] M. Sarsour,[19] S. Sato,[28] S. Sawada,[31] B. Schaefer,[65] B. K. Schmoll,[62] K. Sedgwick,[8] J. Seele,[56]
R. Seidl,[55,56] Y. Sekiguchi,[12] A. Sen,[19,62] R. Seto,[8] P. Sett,[4] A. Sexton,[40] D. Sharma,[61] A. Shaver,[27] I. Shein,[23]
T.-A. Shibata,[55,63] K. Shigaki,[21] M. Shimomura,[27,46] K. Shoji,[55] P. Shukla,[4] A. Sickles,[7,24] C. L. Silva,[38] D. Silvermyr,[39,51]
B. K. Singh,[3] C. P. Singh,[3] V. Singh,[3] M. Skolnik,[43] M. Slunečka,[9] M. Snowball,[38] S. Solano,[43] R. A. Soltz,[37]
W. E. Sondheim,[38] S. P. Sorensen,[62] I. V. Sourikova,[7] P. W. Stankus,[51] P. Steinberg,[7] E. Stenlund,[39] M. Stepanov,[41,‡] A. Ster,[67]
S. P. Stoll,[7] M. R. Stone,[13] T. Sugitate,[21] A. Sukhanov,[7] T. Sumita,[55] J. Sun,[61] J. Sziklai,[67] A. Takahara,[12] A. Taketani,[55,56]
Y. Tanaka,[45] K. Tanida,[56,59] M. J. Tannenbaum,[7] S. Tarafdar,[3,66] A. Taranenko,[47,60] E. Tennant,[49] R. Tieulent,[19] A. Timilsina,[27]
T. Todoroki,[55,64] M. Tomášek,[15,26] H. Torii,[12] C. L. Towell,[1] R. Towell,[1] R. S. Towell,[1] I. Tserruya,[66] H. W. van Hecke,[38]
M. Vargyas,[16] E. Vazquez-Zambrano,[14] A. Veicht,[14] J. Velkovska,[65] R. Vértesi,[67] M. Virius,[15] V. Vrba,[15,26] E. Vznuzdaev,[54]
X. R. Wang,[49,56] D. Watanabe,[21] K. Watanabe,[55,57] Y. Watanabe,[55,56] Y. S. Watanabe,[12,31] F. Wei,[49] S. Whitaker,[27]
A. S. White,[42] S. Wolin,[24] C. L. Woody,[7] M. Wysocki,[51] B. Xia,[50] L. Xue,[19] S. Yalcin,[61] Y. L. Yamaguchi,[12,61] A. Yanovich,[23]
S. Yokkaichi,[55,56] J. H. Yoo,[32] I. Yoon,[59] Z. You,[38] I. Younus,[36,48] H. Yu,[53] I. E. Yushmanov,[33] W. A. Zajc,[14] A. Zelenski,[6]
S. Zhou,[11] and L. Zou[8]
(PHENIX Collaboration)
[1]*Abilene Christian University, Abilene, Texas 79699, USA*
[2]*Department of Physics, Augustana University, Sioux Falls, South Dakota 57197, USA*
[3]*Department of Physics, Banaras Hindu University, Varanasi 221005, India*
[4]*Bhabha Atomic Research Centre, Bombay 400 085, India*
[5]*Baruch College, City University of New York, New York, New York, 10010 USA*
[6]*Collider-Accelerator Department, Brookhaven National Laboratory, Upton, New York 11973-5000, USA*

2469-9985/2016/93(3)/034903(12)

[7]*Physics Department, Brookhaven National Laboratory, Upton, New York 11973-5000, USA*
[8]*University of California-Riverside, Riverside, California 92521, USA*
[9]*Charles University, Ovocný trh 5, Praha 1, 116 36, Prague, Czech Republic*
[10]*Chonbuk National University, Jeonju, 561-756, Korea*
[11]*Science and Technology on Nuclear Data Laboratory, China Institute of Atomic Energy, Beijing 102413, People's Republic of China*
[12]*Center for Nuclear Study, Graduate School of Science, University of Tokyo, 7-3-1 Hongo, Bunkyo, Tokyo 113-0033, Japan*
[13]*University of Colorado, Boulder, Colorado 80309, USA*
[14]*Columbia University, New York, New York 10027 and Nevis Laboratories, Irvington, New York 10533, USA*
[15]*Czech Technical University, Zikova 4, 166 36 Prague 6, Czech Republic*
[16]*ELTE, Eötvös Loránd University, H-1117 Budapest, Pázmány P. s. 1/A, Hungary*
[17]*Ewha Womans University, Seoul 120-750, Korea*
[18]*Florida State University, Tallahassee, Florida 32306, USA*
[19]*Georgia State University, Atlanta, Georgia 30303, USA*
[20]*Hanyang University, Seoul 133-792, Korea*
[21]*Hiroshima University, Kagamiyama, Higashi-Hiroshima 739-8526, Japan*
[22]*Department of Physics and Astronomy, Howard University, Washington, DC 20059, USA*
[23]*IHEP Protvino, State Research Center of Russian Federation, Institute for High Energy Physics, Protvino, 142281, Russia*
[24]*University of Illinois at Urbana-Champaign, Urbana, Illinois 61801, USA*
[25]*Institute for Nuclear Research of the Russian Academy of Sciences, prospekt 60-letiya Oktyabrya 7a, Moscow 117312, Russia*
[26]*Institute of Physics, Academy of Sciences of the Czech Republic, Na Slovance 2, 182 21 Prague 8, Czech Republic*
[27]*Iowa State University, Ames, Iowa 50011, USA*
[28]*Advanced Science Research Center, Japan Atomic Energy Agency, 2-4 Shirakata Shirane,*
Tokai-mura, Naka-gun, Ibaraki-ken 319-1195, Japan
[29]*Helsinki Institute of Physics and University of Jyväskylä, P.O.Box 35, FI-40014 Jyväskylä, Finland*
[30]*Károly Róberts University College, H-3200 Gyöngyös, Mátrai út 36, Hungary*
[31]*KEK, High Energy Accelerator Research Organization, Tsukuba, Ibaraki 305-0801, Japan*
[32]*Korea University, Seoul, 136-701, Korea*
[33]*National Research Center "Kurchatov Institute", Moscow, 123098 Russia*
[34]*Kyoto University, Kyoto 606-8502, Japan*
[35]*Laboratoire Leprince-Ringuet, Ecole Polytechnique, CNRS-IN2P3, Route de Saclay, F-91128, Palaiseau, France*
[36]*Physics Department, Lahore University of Management Sciences, Lahore 54792, Pakistan*
[37]*Lawrence Livermore National Laboratory, Livermore, California 94550, USA*
[38]*Los Alamos National Laboratory, Los Alamos, New Mexico 87545, USA*
[39]*Department of Physics, Lund University, Box 118, SE-221 00 Lund, Sweden*
[40]*University of Maryland, College Park, Maryland 20742, USA*
[41]*Department of Physics, University of Massachusetts, Amherst, Massachusetts 01003-9337, USA*
[42]*Department of Physics, University of Michigan, Ann Arbor, Michigan 48109-1040, USA*
[43]*Muhlenberg College, Allentown, Pennsylvania 18104-5586, USA*
[44]*Myongji University, Yongin, Kyonggido 449-728, Korea*
[45]*Nagasaki Institute of Applied Science, Nagasaki-shi, Nagasaki 851-0193, Japan*
[46]*Nara Women's University, Kita-uoya Nishi-machi Nara 630-8506, Japan*
[47]*National Research Nuclear University, MEPhI, Moscow Engineering Physics Institute, Moscow, 115409, Russia*
[48]*University of New Mexico, Albuquerque, New Mexico 87131, USA*
[49]*New Mexico State University, Las Cruces, New Mexico 88003, USA*
[50]*Department of Physics and Astronomy, Ohio University, Athens, Ohio 45701, USA*
[51]*Oak Ridge National Laboratory, Oak Ridge, Tennessee 37831, USA*
[52]*IPN-Orsay, Univ. Paris-Sud, CNRS/IN2P3, Université Paris-Saclay, BP1, F-91406, Orsay, France*
[53]*Peking University, Beijing 100871, People's Republic of China*
[54]*PNPI, Petersburg Nuclear Physics Institute, Gatchina, Leningrad region, 188300, Russia*
[55]*RIKEN Nishina Center for Accelerator-Based Science, Wako, Saitama 351-0198, Japan*
[56]*RIKEN BNL Research Center, Brookhaven National Laboratory, Upton, New York 11973-5000, USA*
[57]*Physics Department, Rikkyo University, 3-34-1 Nishi-Ikebukuro, Toshima, Tokyo 171-8501, Japan*
[58]*Saint Petersburg State Polytechnic University, St. Petersburg, 195251 Russia*
[59]*Department of Physics and Astronomy, Seoul National University, Seoul 151-742, Korea*
[60]*Chemistry Department, Stony Brook University, SUNY, Stony Brook, New York 11794-3400, USA*
[61]*Department of Physics and Astronomy, Stony Brook University, SUNY, Stony Brook, New York 11794-3800, USA*
[62]*University of Tennessee, Knoxville, Tennessee 37996, USA*
[63]*Department of Physics, Tokyo Institute of Technology, Oh-okayama, Meguro, Tokyo 152-8551, Japan*
[64]*Center for Integrated Research in Fundamental Science and Engineering, University of Tsukuba, Tsukuba, Ibaraki 305, Japan*

[65]*Vanderbilt University, Nashville, Tennessee 37235, USA*
[66]*Weizmann Institute, Rehovot 76100, Israel*
[67]*Institute for Particle and Nuclear Physics, Wigner Research Centre for Physics, Hungarian Academy of Sciences (Wigner RCP, RMKI) H-1525 Budapest 114, PO Box 49, Budapest, Hungary*
[68]*Yonsei University, IPAP, Seoul 120-749, Korea*
[69]*University of Zagreb, Faculty of Science, Department of Physics, Bijenička 32, HR-10002 Zagreb, Croatia*

(Received 5 October 2015; published 3 March 2016)

The invariant yields, dN/dy, for J/ψ production at forward rapidity ($1.2 < |y| < 2.2$) in U + U collisions at $\sqrt{s_{_{NN}}} = 193$ GeV have been measured as a function of collision centrality. The invariant yields and nuclear-modification factor R_{AA} are presented and compared with those from Au + Au collisions in the same rapidity range. Additionally, the direct ratio of the invariant yields from U + U and Au + Au collisions within the same centrality class is presented, and used to investigate the role of $c\bar{c}$ coalescence. Two different parametrizations of the deformed Woods-Saxon distribution were used in Glauber calculations to determine the values of the number of nucleon-nucleon collisions in each centrality class, $N_{\rm coll}$, and these were found to give significantly different $N_{\rm coll}$ values. Results using $N_{\rm coll}$ values from both deformed Woods-Saxon distributions are presented. The measured ratios show that the J/ψ suppression, relative to binary collision scaling, is similar in U + U and Au + Au for peripheral and midcentral collisions, but that J/ψ show less suppression for the most central U + U collisions. The results are consistent with a picture in which, for central collisions, increase in the J/ψ yield due to $c\bar{c}$ coalescence becomes more important than the decrease in yield due to increased energy density. For midcentral collisions, the conclusions about the balance between $c\bar{c}$ coalescence and suppression depend on which deformed Woods-Saxon distribution is used to determine $N_{\rm coll}$.

DOI: 10.1103/PhysRevC.93.034903

I. INTRODUCTION

The study of J/ψ production in high-energy heavy-ion collisions is motivated by the prediction that J/ψ formation would be suppressed by color screening effects in the quark gluon plasma (QGP) [1]. But relating J/ψ suppression to the energy densities of the hot matter formed in heavy-ion collisions is complicated by the presence of competing effects that also modify J/ψ production. Competing effects [2] can be divided into cold nuclear matter (CNM) effects and hot matter effects. CNM effects are those that modify the yield or kinematic distributions of J/ψ produced in a nuclear target in the absence of a QGP. They include modification of the parton densities in a nucleus [3–7], breakup of the J/ψ or its $c\bar{c}$ precursor state in the nuclear target due to collisions with nucleons [8–10], transverse momentum broadening due to the $c\bar{c}$ traversing the cold nucleus, and initial-state parton energy loss [11]. CNM effects are expected to be strongly dependent on collision system, collision energy, rapidity, and collision centrality. In hot matter, J/ψ yields can be enhanced by coalescence of $c\bar{c}$ pairs that are initially unbound, but which become bound due to interactions with the medium [12]. At sufficiently high charm production rates, there can be a significant yield of J/ψ from coalescence of a c and $\bar{c}$ from different hard processes.

Precise J/ψ data extending down to zero p_T have been published for Pb + Pb or Au + Au collisions at energies of $\sqrt{s_{_{NN}}} = 17.3$ GeV [13], 62.4 GeV [14,15], 200 GeV [16–18], and 2.76 TeV [19]. The nuclear-modification factor (R_{AA}) of the J/ψ yield in the highest centrality collisions is observed to drop from $\sqrt{s_{_{NN}}} = 17.3-200$ GeV, and then increase strongly between 200 GeV and 2.76 TeV [16,17,19]. The rise in R_{AA} between 200 GeV and 2.76 TeV is well described [20] in magnitude and transverse momentum dependence by models that include coalescence of c and $\bar{c}$ pairs from different hard scattering processes [12,21]. The energy dependence of the modification suggests that J/ψ production, after accounting for the modification due to cold nuclear matter effects [2,8,9], is increasingly suppressed from 17.3–200 GeV by stronger color screening in the increasingly hot QGP. But when the collision energy increases to 2.76 TeV, the rising underlying charm production rate leads to an increasing, and eventually dominant, contribution to the J/ψ cross section from coalescence.

Of the collision energies observed so far the nuclear modification, R_{AA}, for the most central collisions is at a minimum at $\sqrt{s_{_{NN}}} = 200$ GeV, although there is little difference from 62.4 GeV, where the energy density is smaller. The behavior of R_{AA} in the range of energy densities accessed at energies between $\sqrt{s_{_{NN}}} = 200$ GeV in Au + Au collisions and 2.76 TeV in Pb + Pb collisions is not known. The measurement of J/ψ yields in $\sqrt{s_{_{NN}}} = 193$ GeV ^{238}U+^{238}U collisions, the largest system yet studied at RHIC, during the 2012 data taking at the Relativistic Heavy Ion Collider (RHIC) run provides an opportunity to increase the energy density above that for $\sqrt{s_{_{NN}}} = 200$ GeV Au + Au collisions by ~20% [22], and to observe the effect on the measured R_{AA}. In this paper we report the results of measurements of the J/ψ yield in U + U collisions at forward and backward rapidity at $\sqrt{s_{_{NN}}} = 193$ GeV using the PHENIX detector.

II. PHENIX DETECTOR

The U + U data used in this analysis were recorded at RHIC during 2012. The PHENIX detector [23] configuration used is

---

[*] PHENIX cospokesperson: morrison@bnl.gov

[†] PHENIX cospokesperson: jamie.nagle@colorado.edu

[‡] Deceased.

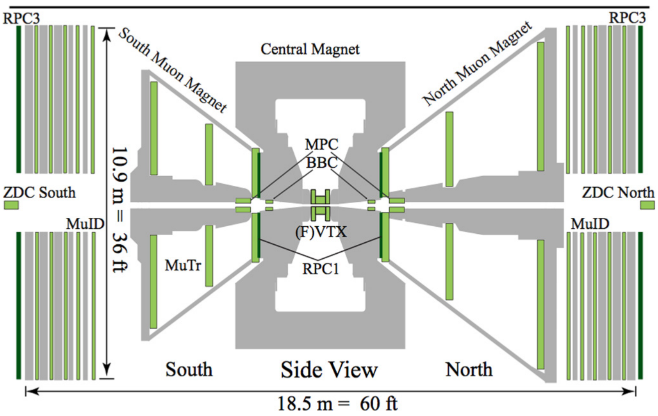

FIG. 1. A schematic side view of the PHENIX muon arms in 2012. The central arms, which are at midrapidity, are not shown.

shown in Fig. 1. The J/ψ yields reported in this paper were all recorded in the muon spectrometers [24].

The minimum-bias trigger was used for this data set. This required two or more hits in each arm of the beam beam counter (BBC), which comprises two quartz arrays of 64 Čerenkov counters, positioned symmetrically in the pseudorapidity range $3.0 < |\eta| < 3.9$. The time difference between the two BBC arms provides the z-vertex position both in the minimum-bias trigger and in the offline analysis.

The J/ψ were reconstructed from their $J/\psi \rightarrow \mu^+\mu^-$ decays, with the muons being detected in two muon spectrometer arms that cover the rapidity ranges $-2.2 < y < -1.2$ (south) and $1.2 < y < 2.4$ (north). Each comprises a magnet, a copper and steel absorber, followed by the muon tracker (MuTr) and the muon identifier (MuID). They are described in detail in Ref. [25]. An additional steel absorber material of thickness 36.2 cm was added in 2010 to improve the muon yield relative to the hadronic background. The muon track momentum is measured in the MuTr, which has three stations, each comprising two or three chambers with two cathode strip planes each, with half of these planes having no stereo angle, and half having their cathode planes tilted at stereo angles that vary between 3 and 11.25 degrees. Discrimination between muons and punch-through hadrons is provided by the MuID, which comprises alternating steel absorber layers interleaved with Iarocci tubes. A muon candidate is required to penetrate all the way to the last layer of the MuID, requiring a minimum muon momentum of 3 GeV/c. The acceptance for the J/ψ, discussed in detail in Sec. III D, is flat to within ≈ 30% from transverse momentum, p_T, of zero to 8 GeV/c.

III. DATA ANALYSIS

For this analysis 1.08×10^9 events with primary vertices within ± 30 cm of the nominal interaction point were analyzed. This corresponds to an integrated luminosity of $\mathcal{L} = 155.6\,\mu\text{b}^{-1}$ and a nucleon-nucleon integrated luminosity of $\int \mathcal{L}_{NN} dt = 238 \times 238 \times 155.6\,\mu\text{b}^{-1} = 8.8\,\text{pb}^{-1}$.

Because the invariant yields in the two muon arms must be identical for the symmetric U + U collision system, the analysis in the north muon arm was restricted to $1.2 < y < 2.2$ to make the rapidity interval equal for the north and south arms.

A. Centrality determination

The centrality determination for U + U collisions is based on the combined charge sum signals from the two BBC detectors. The U + U collisions were modeled using a Monte Carlo simulation based on the Glauber model [26] with a deformed Woods-Saxon distribution for the U nucleus, which accounts for its prolate nature.

$$\rho = \frac{\rho_0}{1 + e^{([r-R']/a)}}, \tag{1}$$

where R' depends on the polar angle θ:

$$R' = R\left[1 + \beta_2 Y_2^0(\theta) + \beta_4 Y_4^0(\theta)\right], \tag{2}$$

and where Y^0 is a Legendre polynomial, ρ_0 is the normal nuclear density, R is the radius of the nucleus, and a is the surface diffuseness parameter.

We considered two parametrizations of the deformed Woods-Saxon distribution for U. The first parameter set, which we call set 1, is from Masui *et al.* [27]. The second, which we call set 2, is from Shou *et al.* [28]. The parameters for the two sets are summarized in Table I.

The parametrization of Shou *et al.* differs from the more conventional one of Masui *et al.* in two ways. First, the finite radius of the nucleon is taken into account. Second, rather than taking the mean radius and diffuseness for the deformed nucleus used in Eqs. (1) and (2) directly from electron scattering experiments, their values are chosen so that after averaging over all orientations of the axis of symmetry for the nucleus, the average radius and diffuseness match the values reported from electron scattering experiments. The result is that the surface diffuseness, a, is considerably smaller for set 2 than for set 1, while the other parameters are similar in value.

The smaller surface diffuseness of set 2 results in a notably more compact nucleus. The total inelastic U + U cross section is 8.3 barns for set 1 and only 7.3 barns for set 2. The result is that the average number of binary collisions is 287 for set 1 and 323 for set 2. Although set 2 appears to have a more consistent usage of the electron scattering data, we note that the neutron skin thickness of large nuclei is not probed via electron scattering and is thus rather unconstrained.

The Glauber model was folded with a negative-binomial distribution, which models the charge production in the rapidity range of the BBC. The parameters of the negative-binomial distribution were fit to the measured charge distribution

TABLE I. Parameters of the deformed Woods-Saxon distribution used in Eqs. (1) and (2).

Parameter	set 1	set 2
$R(fm)$	6.81	6.86
$a(fm)$	0.6	0.42
β_2	0.28	0.265
β_4	0.093	0

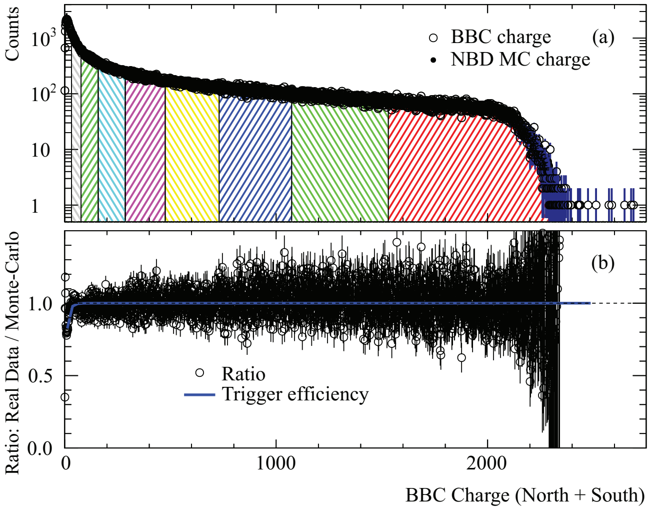

FIG. 2. The BBC charge distribution for U + U collisions for the north and south detectors combined, compared with a Monte Carlo calculation using a negative binomial distribution that is fit to the data. The colored stripes show the BBC charge distribution divided into 10% wide centrality bins.

from the BBC only in the signal range where the BBC minimum-bias trigger is known to be fully efficient. In the low signal range, the efficiency of the trigger was then determined from the ratio of the measured BBC charge distribution to the fitted-negative-binomial distribution. Figure 2 shows the distribution of measured BBC charge. Figure 2(a) shows the measured charge distribution compared with the charge distribution obtained from a Monte Carlo calculation using the fitted-negative-binomial distribution. The efficiency of the BBC trigger was found to be 96 ± 3%. Figure 2(b) shows the ratio of data to the Monte Carlo calculation.

Using the measured BBC charge, the events were divided into 10% wide centrality bins, as illustrated in Fig. 2(a). Due to the limited statistical precision of the data sample, yields were extracted only for centralities from 0-80 %. The mean number of participating nucleons ($N_{\rm part}$) and mean number of nucleon-nucleon collisions ($N_{\rm coll}$) for each centrality bin were found from the Monte Carlo-Glauber calculation. In both cases the Glauber model used a nucleon-nucleon cross section of 42 mb and assumed a hard core radius of 0.4 fm for the distribution of nucleons in the nucleus. The values of these parameters are summarized in Table II for U + U, as determined using deformed Woods-Saxon parameter set 1 and 2.

The systematic uncertainties for the mean $N_{\rm part}$ and $N_{\rm coll}$ values in each centrality bin were estimated by varying the parameters of the Glauber model within reasonable limits. The nucleon-nucleon cross section was varied from 42 mb down to 39 mb and up to 45 mb. For deformed Woods-Saxon parameter set 1 the radius R and diffuseness parameter a were varied down to $R = 6.50$ fm and $a = 0.594$ fm and up to $R = 6.92$ fm and $a = 0.617$ fm. These variations were chosen to match the percentage variations used for the Au + Au case, as were the variations used in the evaluation of systematics for set 2. In addition to these variations of the Glauber model parameters, the calculation was run without using a hard core for the nucleon distribution, and the trigger efficiency was varied within its uncertainty of 3%. For set 1, the uncertainty in the U deformation parameters has been estimated to be approximately 3% for the dipole component β_2 and approximately 50% for the small contribution of the quadrupole component β_4 [29]. Varying β_2 and β_4 by these amounts resulted in an insignificant contribution to the systematic uncertainty for $N_{\rm part}$ and $N_{\rm coll}$. The systematic uncertainties are shown in Table II.

The $N_{\rm part}$ values obtained from the two deformed Woods-Saxon parameter sets are essentially indistinguishable. However the differences between the $N_{\rm coll}$ values obtained from the two parameter sets are, at some centralities, outside the uncertainties on the $N_{\rm coll}$ values. This is due primarily to the large difference in the diffuseness values for the two sets. As noted earlier, the smaller diffuseness for set 2 (0.42 fm vs 0.6 fm for set 1) combined with a similar mean radius results in larger $N_{\rm coll}$ values at all centralities because it makes the nucleus more compact.

Because the $N_{\rm coll}$ values are important in the interpretation of the U + U data, and are directly involved in the calculation of the R_{AA}, we have chosen to consider the $N_{\rm coll}$ values from both sets 1 and 2 in the remainder of the paper.

B. Muon-track and pair reconstruction

Muon candidates are charged particle tracks, which penetrate all layers of the MuID. These MuID tracks are matched to MuTr tracks, which provide the momentum measurement.

TABLE II. Centrality parameters $N_{\rm part}$ and $N_{\rm coll}$ in U + U (this work) and Au + Au [16] collisions, estimated using the Glauber model. The systematic uncertainties are shown, and were estimated as described in the text.

	U + U set 1		U + U set 2		Au + Au	
Centrality	$N_{\rm part}$	$N_{\rm coll}$	$N_{\rm part}$	$N_{\rm coll}$	$N_{\rm part}$	$N_{\rm coll}$
0%–10%	386 ± 5.2	1161 ± 126	387 ± 5.5	1228 ± 142	326 ± 3.9	962 ± 97
10%–20%	273 ± 6.7	708 ± 69	274 ± 6.4	770 ± 86	236 ± 5.5	609 ± 60
20%–30%	190 ± 6.6	426 ± 42	192 ± 6.7	473 ± 52	168 ± 5.8	378 ± 37
30%–40%	128 ± 6.7	244 ± 24	130 ± 6.5	277 ± 29	116 ± 5.8	224 ± 23
40%–50%	81.9 ± 6.4	130 ± 16	83.0 ± 6.2	149 ± 18	76.2 ± 5.5	125 ± 15
50%–60%	47.7 ± 5.4	61.7 ± 10	48.5 ± 5.3	71.0 ± 11.3	47.1 ± 4.8	63.9 ± 9.4
60%–70%	24.7 ± 4.0	25.8 ± 5.3	25.3 ± 3.9	29.3 ± 6.0	26.7 ± 3.7	29.8 ± 5.4
70%–80%	10.9 ± 2.3	9.2 ± 2.4	11.2 ± 2.4	10.2 ± 2.8	13.7 ± 2.5	12.6 ± 2.8

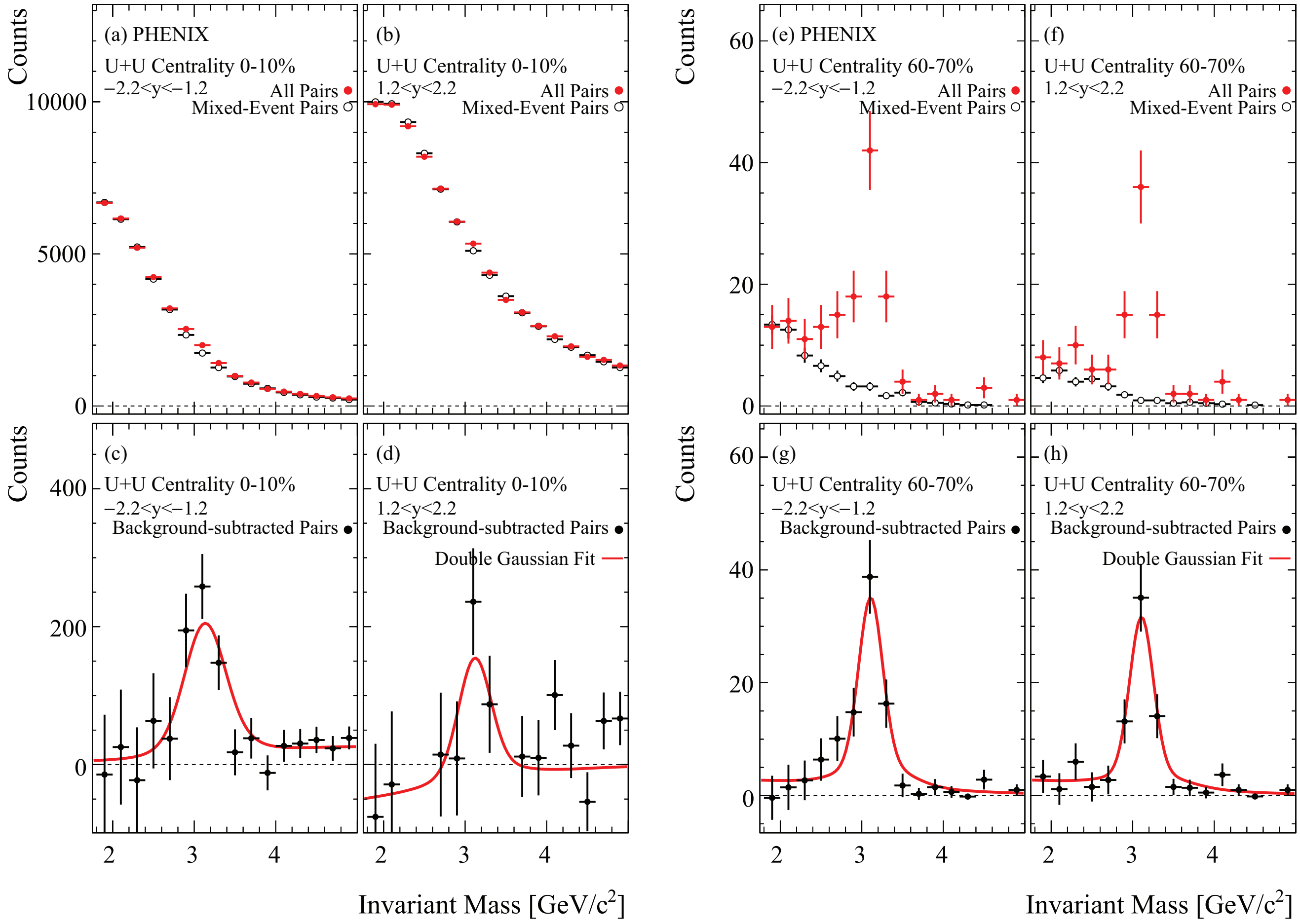

FIG. 3. Dimuon invariant mass spectra at forward and backward rapidity measured in the 0–10% most central collisions [(a)–(d)] and in 60–70% midperipheral collisions [(e)–(h)], integrated over the full p_T range. (a), (b), (e), and (f) show the invariant mass distribution, reconstructed from (solid symbols) same-event opposite charge-sign pairs and (open symbols) mixed-event pairs in U + U collisions. (c), (d), (g), and (h) show the combinatorial background subtracted mass spectra. The solid line is a fit to the data using a double Gaussian line shape plus an exponential background, as described in the text.

Although the requirement that tracks pass through the whole spectrometer arm reduces significantly the hadron contribution, a small percentage of charged hadrons can travel through without interacting (∼0.1%), and these are a source of background. Some muons produced from charged hadron decays in front of the MuTr are also reconstructed, and form a background of real muons in the spectrometer arms. Various offline analysis selection criteria are used to enhance the sample of good muon candidate tracks. There is a cut on the single track χ^2, and also on the difference in position and angle between the extrapolated MuTr and MuID parts of the candidate track. During the dimuon reconstruction, the selected track pair is fit with the event z-vertex position, and a second χ^2 cut is applied for the track pair fit.

C. $\mu^+ + \mu^-$ analysis

The invariant mass distribution is formed by combining all pairs of oppositely charged muon tracks. There is a significant combinatorial background under the J/ψ peak that is formed by single muons or misidentified hadrons that randomly combine to form a pair. There is also a continuum due to correlated muons from semileptonic decays of open charm and bottom, and correlated muons from the Drell-Yan process. The combinatorial background may be estimated by event mixing, in which tracks with opposite charges from different events (of similar z vertex and centrality) are combined randomly, see Ref. [16] for more details. By construction, such mixing destroys any real muon correlations, and so the mixed event background does not reproduce the correlated background from physics sources.

Figures 3(a)–3(h) show the dimuon spectra from the south and north spectrometer arms for two example centrality bins and the combinatorial-background-subtracted mass spectra. The mixed-event combinatorial background is normalized to the real data using yields of muon pairs having the same charge sign found in both the mixed-pairs and real-pairs data samples in a range close to the J/ψ mass peak region, $2.6 < M < 3.6$ GeV/c^2. The procedure is similar to that described in Ref. [30]. Because the mass resolution precludes the separation of the J/ψ and ψ' peaks in this analysis, we present only J/ψ results in this paper.

The J/ψ yield was obtained using a fit in the mass range 1.7–5 GeV/c^2. The fitting function included the mixed event background, a signal line shape, and an exponential. The signal line shape for the J/ψ was a double Gaussian line shape modified by the mass dependence of the muon arm acceptance. The exponential was used to account for the correlated background that is not described by the mixed-event background, and to compensate for any systematic effects from undersubtracting or oversubtracting the large combinatorial background. Because of the limited statistical sample for the U + U measurement, the form of the signal line shape was based on studies of the mass spectrum in p + p collisions, with input from studies performed for the Cu + Au system [31] where the J/ψ mass width was found to increase linearly with increasing multiplicity in the muon arms. The functional form of the increase of the width with collision centrality was found independently for each muon arm from Cu + Au collision data, taken in the same RHIC data-taking period. This was then extrapolated where necessary to the higher multiplicity for the U + U system. As a cross check, a similar increase of the widths with multiplicity was observed in a GEANT [32] Monte Carlo calculation with simulated PYTHIA [33] J/ψ events embedded into real U + U data events. The mass width varies from (peripheral to central) 0.14–0.2 GeV/c^2 for the south arm, and from (peripheral to central) 0.14–0.24 GeV/c^2 in the north arm.

Because the width was fixed at each centrality by this procedure, the J/ψ yield was the only free parameter in the line shape. The fit is shown in Figs. 3(c), 3(d), 3(g), and 3(h). The systematic uncertainty on the yield from the fit was estimated by varying the mass fit range, varying the relative normalization of the signal to the mixed-event combinatorial background by ±2%, and also extracting the yield by using a like-sign combinatorial background in the fit instead of the mixed-event background. Additional systematic checks were made by comparing the yields to those obtained from the raw signal count after exponential background subtraction, and to those obtained from other fit functions. The latter included allowing the Gaussian widths of the J/ψ peak to be free in the fit function, where it was found that the yields agreed within the statistical uncertainty. The systematic uncertainty from the fit was larger in the north arm than in the south arm. For both arms, the fit systematic uncertainties were estimated to range from 0.8% for peripheral events to 10.9% for central events.

D. Efficiency and corrections

The J/ψ detection efficiency was estimated in a two-step process. First, the efficiency to detect hits in each plane of the MuID was estimated by finding all roads made by charged particles through the MuID, but ignoring hits in the plane of interest. The efficiency for the plane of interest was then estimated from the number of roads with associated hits in that plane compared with all roads ignoring hits in that plane. Because the MuID efficiency decreases with increasing luminosity, the final efficiency used was the luminosity weighted average over all runs used in this analysis. The MuID efficiency is included in the calculation of the acceptance ⊗ reconstruction efficiency described below.

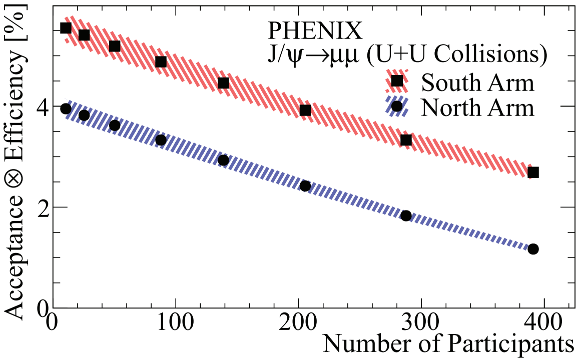

FIG. 4. Acceptance ⊗ efficiency as a function of collision centrality (N_{part}) for (squares) south arm, $-2.2 < y < -1.2$ and (circles) north arm, $1.2 < y < 2.2$. The bands represent the uncertainty due to the limited statistical precision of the embedding simulations.

The full acceptance ⊗ efficiency (acceptance convoluted with efficiency) is estimated by embedding PYTHIA $J/\psi \rightarrow \mu^+\mu^-$ decays—fully simulated via a GEANT description of the PHENIX detector—into a reference data sample. The data plus simulation is then reconstructed with the same analysis as the real data and the final acceptance ⊗ efficiency is evaluated, normalized by the number of simulated $J/\psi \rightarrow \mu^+\mu^-$ decays over the same rapidity range.

The acceptance ⊗ efficiency for J/ψ in U + U collisions is shown in Fig. 4. As observed for other collision systems, the north arm has lower efficiency than the south, and the efficiency is strongly centrality dependent. These factors are reflected in the final data yields, where the statistical uncertainties are largest for the north arm, and increase with increasing centrality.

Between the measurement of the p + p data [34] used as the reference for the U + U nuclear modification (see Sec. IV A) and the U + U data, additional absorber material was added in front of the muon arms. The added absorber increases the minimum energy required for a muon to penetrate to the last gap of the MuID detector, and this reduces the J/ψ acceptance near $y = 1.2$ at low p_T. Because a realistic rapidity shape (from PYTHIA) is used when calculating the rapidity integrated acceptance ⊗ efficiency, it should be correct for both the U + U and p + p measurements. We note that the systematic uncertainty for the U + U acceptance ⊗ efficiency includes an uncertainty due to the possible deviation of the U + U rapidity shape from that given by PYTHIA, as discussed in Sec. III E.

E. Systematic uncertainties

The systematic uncertainties are divided into three groups: Type A, point-to-point uncorrelated uncertainties; Type B, point-to-point correlated uncertainties; and Type C, global scale uncertainties, which are summarized in Table III. The signal extraction systematic uncertainty due to the fitting procedure, discussed in Sec. III C, is treated as a Type A uncertainty. The uncertainty arising from the assumptions about the input J/ψ momentum and rapidity distributions used in the PYTHIA calculations were previously studied in Ref. [14] and were found to be ∼4.0%. The uncertainty in the detector

TABLE III. Estimated systematic uncertainties.

Source	Uncertainty (%)	Type
J/ψ signal extraction	$\pm$ 0.8–10.9	A
input J/ψ p_T distributions	$\pm$ 4.0	B
detector acceptance	$\pm$ 5.0	B
reconstruction and trigger efficiency	$\pm$ 5.0	B
run-to-run efficiency variation	$\pm$ 2.8	B
Glauber ($N_{\rm coll}$)	$\pm$ 10.8–33.0	B
p + p reference	$\pm$ 7.1	C
p + p reference energy scale	$\pm$ 3.6	C

acceptance is estimated to be ∼5.0%. An overall uncertainty on the reconstruction and trigger efficiency obtained from embedding PYTHIA events in real data is estimated to be ∼5.0%. Small run-to-run variations in the MuID and MuTr efficiency were studied in Ref. [31] and found to be 2.8%. The uncertainty in the mean $N_{\rm coll}$ values for the centrality bins was studied as described in Sec. III A, and found to be 10.8–33.0% (see Table II). The measured p + p reference invariant yield contributes a systematic uncertainty of 7.1%. This is smaller than the p + p global systematic uncertainty because both the BBC trigger efficiency for p + p and the $N_{\rm coll}$ estimate used in the R_{AA} depend on the assumed nucleon-nucleon cross section, and so their systematic uncertainties cancel in part when forming R_{AA}. An additional small systematic uncertainty is assigned to the p + p reference for the nuclear-modification factor because the p + p cross section, measured at $\sqrt{s} = 200$ GeV, had to be extrapolated to $\sqrt{s} = 193$ GeV to obtain the reference cross section for the U + U data set. That systematic uncertainty was taken conservatively to be equal to the correction, 3.6%, and when it is added in quadrature with the 7.1% from the p + p reference measurement, the overall global uncertainty due to the p + p reference becomes 8.1%.

IV. RESULTS

The J/ψ yields measured in the two muon arms agree well, within statistical uncertainties. Therefore the U + U results presented here are averaged over both forward and backward rapidity.

A. Yield and R_{AA} versus $N_{\rm part}$

The measured invariant yield is obtained from Eq. (3):

$$B_{\mu\mu}\frac{dN}{dy} = \frac{1}{N_{\rm event}}\frac{N^{J/\psi}_{\rm measured}}{\Delta y A\epsilon}, \tag{3}$$

where B is the branching fraction for J/ψ decay to dimuons, $N^{J/\psi}_{\rm measured}$ is the measured number of J/ψ integrated over all p_T, $N_{\rm event}$ is the number of minimum-bias events analyzed, $A\epsilon$ is the acceptance ⊗ efficiency, and Δy is the rapidity range used when calculating the acceptance of the muon arms.

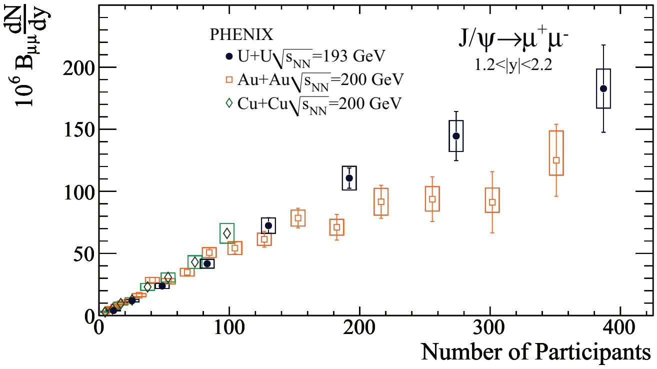

FIG. 5. Invariant yield of the J/ψ at forward rapidity measured as a function of collision centrality ($N_{\rm part}$) for (closed circles) U + U, (open squares) Au + Au [16], and (open diamonds) Cu + Cu [35].

The invariant yield for J/ψ production in U + U collisions at $\sqrt{s_{NN}} = 193$ GeV is shown versus $N_{\rm part}$ in Fig. 5, where the vertical error bars represent the statistical uncertainty plus Type A systematic uncertainty for the yield extraction, added in quadrature. The boxes represent the Type B systematic uncertainties, summed in quadrature. In addition to U + U, the largest system measured at RHIC, the $N_{\rm part}$ dependence of the invariant yield is shown for two other symmetric systems, Au + Au [16] and Cu + Cu [35] at $\sqrt{s_{NN}} = 200$ GeV. The yields below $N_{\rm part} \approx 150$ are similar for all three systems at the same $N_{\rm part}$. However for $N_{\rm part} \gtrsim 200$ the yield for U + U is larger than that for Au + Au.

The departure from unity of the nuclear-modification factor,

$$R_{AA} = \frac{1}{\langle N_{\rm coll}\rangle}\frac{dN^{AA}/dy}{dN^{pp}/dy}, \tag{4}$$

quantifies the modification of the $N_{\rm coll}$ normalized invariant yield in heavy-ion collisions relative to the invariant yield in p + p collisions. The reference p + p invariant yield was obtained from Ref. [34]. Because the p + p data were measured at $\sqrt{s} = 200$ GeV a scale factor of 0.964, determined from p + p PYTHIA simulations at $\sqrt{s} = 193$ GeV and $\sqrt{s} = 200$ GeV, was applied to the p + p invariant yield to account for the difference in J/ψ cross section.

As discussed in Sec. III A, the deformed Woods-Saxon parameter sets 1 and 2 are derived using different assumptions, resulting in substantially different values of the surface diffuseness parameter, a. The authors of Ref. [28] argue that their approach in producing parameter set 2 corrects deficiencies in the conventional method, and is the correct one. In any case, both assumptions cannot be correct, so the differences in the deformed Woods-Saxon parameters between the two sets do not represent a systematic uncertainty on the R_{AA}, because one set is correct (within its uncertainties) and the other is not. We have chosen to present the R_{AA} calculated using both sets, so that the effect of using a conventional description and the description of reference [28] of the deformed U nucleus can be compared.

The nuclear-modification factor for U + U collisions is shown as a function of $N_{\rm part}$ in Fig. 6. Figure 6(a) shows the R_{AA} calculated using $N_{\rm coll}$ values from deformed Woods-Saxon parameter set 1. Figure 6(b) shows the R_{AA} calculated using those from parameter set 2. The vertical bars represent the combined statistical and Type A systematic uncertainties and the boxes represent the Type B uncertainties. The Type

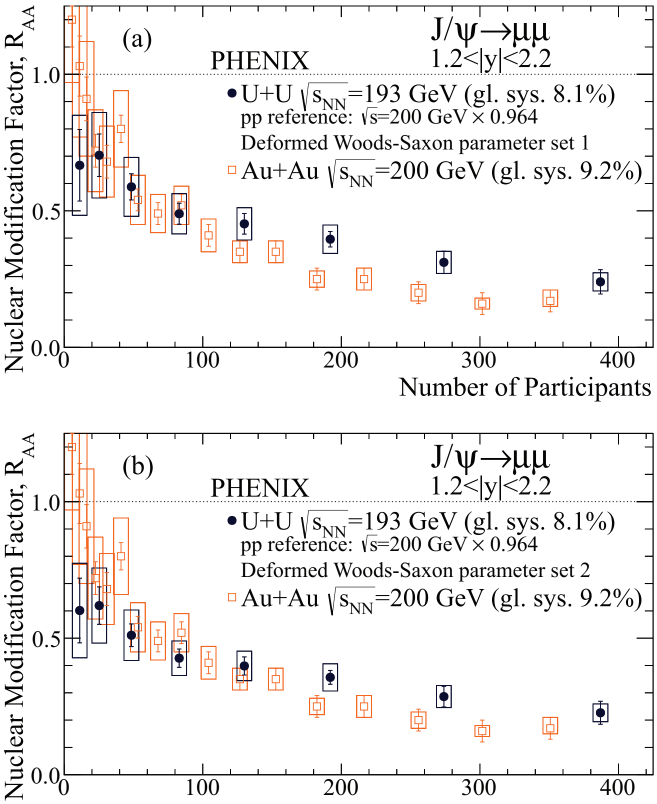

FIG. 6. The nuclear-modification factor, R_{AA}, measured as a function of collision centrality (N_{part}) for (closed circles) J/ψ at forward rapidity in U + U collisions, for which the p + p reference data, measured at $\sqrt{s} = 200$ GeV, has been scaled down by a factor 0.964 to account for the difference in J/ψ cross section between $\sqrt{s} = 200$ and 193 GeV; (open squares) Au + Au data [16]. (a) The U + U R_{AA} calculated using Woods-Saxon parameter set 1 [27] in the U + U Glauber model calculation. (b) The U + U R_{AA} calculated using parameter set 2 [28].

C (global) uncertainties are listed in the legend. The overall global uncertainty (Type C) is 8.1%. The modification for Au + Au collisions [16] is shown for comparison. The R_{AA} values for U + U collisions are provided in Table IV.

The measured R_{AA} for the U + U collision system is similar to that for the Au + Au system, although the U + U data for the most central collisions show less modification than the Au + Au data.

B. Yield and R_{AA} versus collision centrality

Possible effects that may modify J/ψ production in U + U collisions with respect to Au + Au collisions were discussed in Ref. [22]. The expected higher energy density in U + U compared to Au + Au (15–20%) should lead to a stronger suppression due to color screening. On the other hand, for a given centrality, a larger N_{coll} value in U + U (compared to Au + Au) should increase charm production by $c\bar{c}$ coalescence. Cold nuclear matter effects due to shadowing are expected to be similar in both systems.

TABLE IV. The nuclear-modification factor (R_{AA}) for U + U collisions [averaged over forward ($1.2 < y < 2.2$) and backward ($-2.2 < y < -1.2$) rapidity], as a function of centrality, derived from deformed Woods-Saxon parameter sets 1 and 2 (see text for details). The first and second uncertainties listed represent Type-A (statistical uncertainties plus point-to-point systematic uncertainties from the yield extraction) and Type-B uncertainties, respectively (see text for definitions). There is a Type-C (global) systematic uncertainty of 8.1%.

Centrality	R_{UU} (set 1)	R_{UU} (set 2)
0%–10%	$0.240 \pm 0.045 \pm 0.031$	$0.225 \pm 0.042 \pm 0.031$
10%–20%	$0.314 \pm 0.041 \pm 0.035$	$0.285 \pm 0.038 \pm 0.035$
20%–30%	$0.400 \pm 0.028 \pm 0.044$	$0.349 \pm 0.025 \pm 0.044$
30%–40%	$0.463 \pm 0.039 \pm 0.053$	$0.390 \pm 0.033 \pm 0.053$
40%–50%	$0.513 \pm 0.040 \pm 0.070$	$0.410 \pm 0.032 \pm 0.070$
50%–60%	$0.604 \pm 0.049 \pm 0.109$	$0.477 \pm 0.039 \pm 0.109$
60%–70%	$0.698 \pm 0.077 \pm 0.165$	$0.567 \pm 0.063 \pm 0.165$
70%–80%	$0.646 \pm 0.137 \pm 0.241$	$0.529 \pm 0.104 \pm 0.241$

As suggested in Ref. [22], we define for a given centrality class the relative nuclear-modification factor

$$R_{\text{AuAu}}^{UU} = \frac{dN^{UU}/dy}{dN^{\text{AuAu}}/dy}\left(\frac{N_{\text{coll}}^{\text{AuAu}}}{0.964 \times N_{\text{coll}}^{UU}}\right)^2, \tag{5}$$

where N_{coll}^{UU} is the mean value of N_{coll} in the given centrality class (e.g., 10–20%) in U + U collisions, and $N_{\text{coll}}^{\text{AuAu}}$ is the corresponding value for Au + Au collisions in the same centrality class. The N_{coll}^2 ratio in Eq. (5) is intended to account for the expected scaling of the J/ψ cross section with N_{coll}^2 in the case of $c\bar{c}$ coalescence. This assumes that the coalescence yield depends on the number of charm quarks squared, and thus on the number of binary collisions squared. However to get the correct scaling in this case, the values of N_{coll} for U + U have to be modified by a factor 0.964 because the charm production cross section in p + p collisions at $\sqrt{s} = 193$ GeV is smaller than that at $\sqrt{s} = 200$ GeV by that factor.

If the production of J/ψ in central collisions was entirely due to $c\bar{c}$ coalescence, and if cold nuclear matter effects were the same for both systems, the relative nuclear modification would be expected to be 1. The variable has the advantage that it is a direct ratio of U + U and Au + Au invariant yields, eliminating the systematic uncertainties associated with the p + p reference when forming the R_{AA}. The ratio of N_{coll}^2 values for Au + Au and U + U also appears in R_{AuAu}^{UU}. But the systematic uncertainty estimation for U + U (see Sec. III A) was carried out in such a way that the systematic uncertainties in N_{coll} are highly correlated for U + U and Au + Au, and they mostly cancel when taking the ratio of N_{coll} values. There is still, however, the large difference in the diffuseness parameter, a, coming from the difference between the models used to obtain parameter sets 1 and 2. We deal with that by calculating R_{AuAu}^{UU} for both models.

The invariant yield is shown plotted versus centrality class for U + U and Au + Au in Fig. 7. To form the relative nuclear modification of Eq. (5), some rebinning of the Au + Au data is required. The rebinned invariant yields and their ratios are

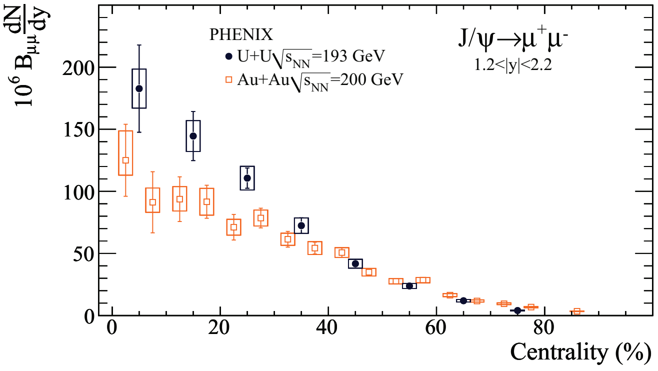

FIG. 7. Invariant yield measured as a function of collision centrality for J/ψ at forward rapidity for (closed circles) U + U and (open squares) Au + Au [16] collisions.

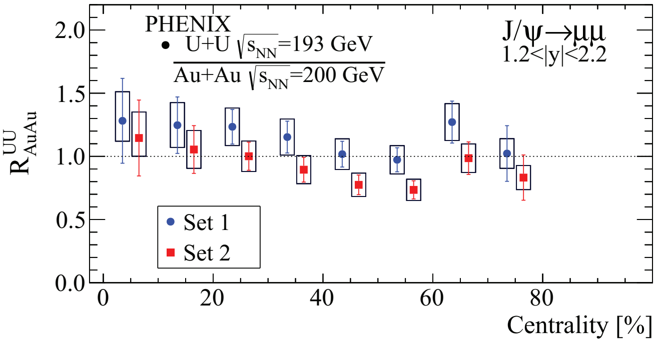

FIG. 8. The relative nuclear-modification factor for U + U and Au + Au [Eq. (5)] as a function of collision centrality. Values were calculated using N_{coll} values obtained from the U + U Glauber model calculation using Woods-Saxon parameter set 1 [27] and set 2 [28]. The values for set 1 and set 2 are slightly offset in centrality for clarity.

summarized in Table V. Because the U + U and Au + Au data were taken in different years, and there were differences in the muon arm absorber thickness due to an upgrade, all of the systematic uncertainties on the invariant yields are propagated in the ratio.

The values of R^{UU}_{AuAu} are plotted in Fig. 8, and summarized in Table VI. For the N_{coll} values from set 2, the relative nuclear modification falls below one for collisions in the 40–60% region, but rises to one for the most central collisions. For N_{coll} values from set 1, the relative nuclear modification is slightly above 1 for central collisions and approximately one across the remainder of the centrality range. These results suggest that the invariant yield scales with $N_{\text{coll}}{}^2$ for the most central collisions, at least.

As a different way of looking at the data, we show in Fig. 9 the ratio of the invariant yields for U + U and Au + Au, taken from Table V. These do not depend on N_{coll}. For comparison, in Fig. 9 we also present curves showing how the ratio would depend on centrality if it scaled with N_{coll} (dashed curve) or with $N_{\text{coll}}{}^2$ (solid curve). As in Eq. (5), the values of N_{coll} for U + U are multiplied by 0.964 to account for the difference in cross section for J/ψ production in p + p collisions at 193 GeV and 200 GeV collision energy. When N_{coll} values from set 2 are used, the measured ratios for midcentral collisions lie at or below the ratio of N_{coll} values, but as the collision centrality increases the data points move above the ratio of N_{coll} values until, for the most central collisions, they favor the $N_{\text{coll}}{}^2$ curve. When N_{coll} values from set 1 are used, the data slightly favor the trend of the $N_{\text{coll}}{}^2$ curve across the centrality range.

These comparisons of the ratios of the U + U and Au + Au invariant yields with N_{coll} values derived from both deformed Woods-Saxon parameter sets suggests that, for central collisions, increased $c\bar{c}$ coalescence is more important than stronger suppression due to increased energy density. When the N_{coll} values from set 2 are used, the peripheral and midcentral data suggest that the increased suppression due to increased energy density and increased coalescence due to larger underlying charm yields approximately cancel each other. When the N_{coll} values from set 1 are used, the peripheral and midcentral ratios are consistent with either N_{coll} or $N_{\text{coll}}{}^2$ scaling.

V. SUMMARY

We have presented measurements of the p_T integrated invariant yield dN/dy and nuclear modification R_{AA} for J/ψ production in U + U collisions at $\sqrt{s_{NN}} = 193$ GeV, and compared them with existing data for Au + Au collisions at $\sqrt{s_{NN}} = 200$ GeV. In addition to comparing the invariant yields and nuclear modification, R_{AA}, for the two systems, we have combined them to form the relative nuclear modification,

TABLE V. The invariant yield for U + U collisions [averaged over forward ($1.2 < y < 2.2$) and backward ($-2.2 < y < -1.2$) rapidity], the invariant yield for Au + Au collisions, and the ratio of invariant yields plotted in Fig. 9, all as a function of centrality. The first and second uncertainties listed represent Type-A (statistical uncertainties plus point-to-point systematic uncertainties from the yield extraction) and Type-B uncertainties, respectively (see text for definitions). There is no Type-C (global) systematic uncertainty for the invariant yield.

Centrality	$10^6 B_{\mu\mu} dN^{UU}/dy$	$10^6 B_{\mu\mu} dN^{\text{AuAu}}/dy$	$\frac{dN^{UU}/dy}{dN^{\text{AuAu}}/dy}$
0%–10%	$182.7 \pm 35.1 \pm 15.7$	$105.3 \pm 18.8 \pm^{16.6}_{9.72}$	$1.73 \pm 0.46 \pm^{0.31}_{0.22}$
10%–20%	$144.5 \pm 19.8 \pm 12.4$	$92.3 \pm 10.7 \pm^{10.6}_{10.3}$	$1.57 \pm 0.28 \pm 0.22$
20%–30%	$110.6 \pm 8.2 \pm 9.5$	$75.8 \pm 6.3 \pm 6.4$	$1.46 \pm 0.16 \pm 0.18$
30%–40%	$72.4 \pm 6.3 \pm 6.2$	$56.8 \pm 3.8 \pm 5.1$	$1.27 \pm 0.14 \pm 0.16$
40%–50%	$41.7 \pm 3.4 \pm 3.6$	$40.5 \pm 2.4 \pm 3.4$	$1.03 \pm 0.10 \pm 0.12$
50%–60%	$23.8 \pm 2.0 \pm 2.0$	$28.2 \pm 1.4 \pm 2.1$	$0.84 \pm 0.08 \pm 0.10$
60%–70%	$11.9 \pm 1.4 \pm 1.0$	$13.4 \pm 0.8 \pm 1.0$	$0.89 \pm 0.12 \pm 0.10$
70%–80%	$4.0 \pm 0.8 \pm 0.4$	$7.9 \pm 0.54 \pm 0.60$	$0.51 \pm 0.11 \pm 0.06$

TABLE VI. The relative nuclear-modification factor for U + U and Au + Au collisions [see Eq. (5)] [averaged over forward ($1.2 < y < 2.2$) and backward ($-2.2 < y < -1.2$) rapidity]. The values derived from the deformed Woods-Saxon parameter sets 1 [27] and 2 [28] are shown. The first and second uncertainties listed represent Type-A (statistical uncertainties plus point-to-point systematic uncertainties from the yield extraction) and Type-B uncertainties, respectively (see text for definitions). There is no Type-C (global) systematic uncertainty.

Centrality	R^{UU}_{AuAu} (set 1)	R^{UU}_{AuAu} (set 2)
0%–10%	$1.29 \pm 0.34 \pm^{0.23}_{0.16}$	$1.13 \pm 0.30 \pm^{0.20}_{0.14}$
10%–20%	$1.27 \pm 0.23 \pm 0.18$	$1.04 \pm 0.19 \pm 0.15$
20%–30%	$1.26 \pm 0.14 \pm 0.15$	$0.96 \pm 0.11 \pm 0.12$
30%–40%	$1.21 \pm 0.13 \pm 0.15$	$0.86 \pm 0.09 \pm 0.11$
40%–50%	$1.12 \pm 0.11 \pm 0.13$	$0.72 \pm 0.07 \pm 0.09$
50%–60%	$1.03 \pm 0.10 \pm 0.12$	$0.64 \pm 0.06 \pm 0.07$
60%–70%	$1.25 \pm 0.16 \pm 0.14$	$0.83 \pm 0.11 \pm 0.10$
70%–80%	$0.96 \pm 0.21 \pm 0.11$	$0.64 \pm 0.14 \pm 0.07$

R^{UU}_{AuAu} [22]. The relative nuclear modification [Eq. (5)] was proposed as a way to eliminate the systematic uncertainties associated with the formation of R_{AA}, and to cancel most of the systematic uncertainties associated with the number of binary nucleon collisions, N_{coll}. It is designed to have a value of one if the J/ψ cross section is dominated by $c\bar{c}$ coalescence. We have also compared the ratio of the invariant yields for U + U and Au + Au with the ratio of N_{coll} values and the ratio of ${N_{\mathrm{coll}}}^2$ values for U + U and Au + Au.

We discussed the effect of using two different parametrizations for the deformed Woods-Saxon distribution on the estimates of N_{coll} for U + U collisions. A recently proposed method for estimating the Glauber model parameters (set 2) [28] leads to a smaller surface diffuseness for U, and thus larger values of N_{coll}, than a conventional estimate (set 1) [27]. We presented R_{AA} values and relative nuclear modification values obtained using N_{coll} values from both deformed Woods-Saxon parameter sets.

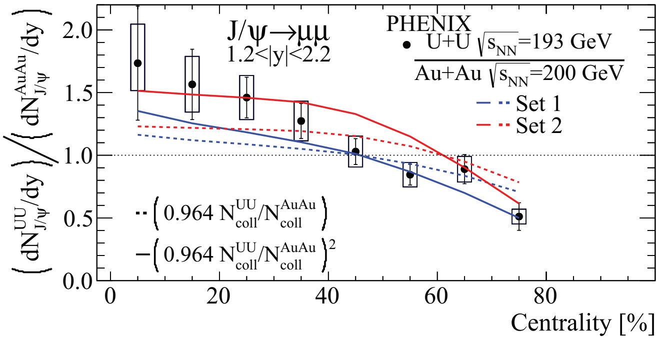

FIG. 9. The ratio of the invariant yield for U + U to that for Au + Au, as a function of collision centrality. The curves show how the ratio would vary with centrality if the invariant yield scaled with N_{coll} (dashed curve) or with ${N_{\mathrm{coll}}}^2$ (solid curve). The N_{coll} ratio curves obtained from the U + U Glauber model calculation using Woods-Saxon parameter set 1 [27] are shown in blue, those using parameter set 2 [28] are shown in red. The N_{coll} value for U + U is multiplied by a factor of 0.964 to account for the decrease of the charm cross section for p + p collisions from 200 GeV to 193 GeV collision energy.

For both sets of N_{coll} values the R_{AA} for U + U is found to be less suppressed than for Au + Au in central collisions that have a similar number of participants. The relative nuclear modification is found to be one for the most central collisions for both N_{coll} sets, but for set 2 it falls below one for midperipheral and peripheral collisions. When the ratios of invariant yields are compared with the ratios of N_{coll} and ${N_{\mathrm{coll}}}^2$ values, they are found to show a slight preference for ${N_{\mathrm{coll}}}^2$ scaling for central collisions.

For both sets of N_{coll} values the behavior is consistent with a picture in which, for central collisions, the increase in J/ψ yield for U + U due to $c\bar{c}$ coalescence becomes more important than the decrease in yield due to increased energy density. For N_{coll} values from set 1, the results are consistent with both N_{coll} and ${N_{\mathrm{coll}}}^2$ scaling for midperipheral collisions. For N_{coll} values from set 2, the results suggest that in the 40%–60% centrality range the increased suppression due to higher energy density in U + U collisions is more important than the increased J/ψ yield due to coalescence caused by the higher underlying charm production.

ACKNOWLEDGMENTS

We thank the staff of the Collider-Accelerator and Physics Departments at Brookhaven National Laboratory and the staff of the other PHENIX participating institutions for their vital contributions. We acknowledge support from the Office of Nuclear Physics in the Office of Science of the Department of Energy, the National Science Foundation, Abilene Christian University Research Council, Research Foundation of SUNY, and Dean of the College of Arts and Sciences, Vanderbilt University (U.S.A.), Ministry of Education, Culture, Sports, Science, and Technology and the Japan Society for the Promotion of Science (Japan), Conselho Nacional de Desenvolvimento Científico e Tecnológico and Fundação de Amparo à Pesquisa do Estado de São Paulo (Brazil), Natural Science Foundation of China (People's Republic of China), Croatian Science Foundation and Ministry of Science, Education, and Sports (Croatia), Ministry of Education, Youth and Sports (Czech Republic), Centre National de la Recherche Scientifique, Commissariat à l'Énergie Atomique, and Institut National de Physique Nucléaire et de Physique des Particules (France), Bundesministerium für Bildung und Forschung, Deutscher Akademischer Austauschdienst, and Alexander von Humboldt Stiftung (Germany), National Science Fund, OTKA, Károly Róbert University College (Hungary) Department of Atomic Energy and Department of Science and Technology (India), Israel Science Foundation (Israel), Basic Science Research Program through NRF of the Ministry of Education (Korea), Physics Department, Lahore University of Management Sciences (Pakistan), Ministry of Education and Science, Russian Academy of Sciences, Federal Agency of Atomic Energy (Russia), VR and Wallenberg Foundation (Sweden), the U.S. Civilian Research and Development Foundation for the Independent States of the Former Soviet Union, the Hungarian American Enterprise Scholarship Fund, and the US-Israel Binational Science Foundation.

[1] T. Matsui and H. Satz, J/ψ Suppression by quark-gluon plasma formation, Phys. Lett. B **178**, 416 (1986).

[2] N. Brambilla, S. Eidelman, B. K. Heltsley, R. Vogt, G. T. Bodwin *et al.*, Heavy quarkonium: progress, puzzles, and opportunities, Eur. Phys. J. C **71**, 1534 (2011).

[3] M. Hirai, S. Kumano, and T. -H. Nagai, Determination of nuclear parton distribution functions and their uncertainties in next-to-leading order, Phys. Rev. C **76**, 065207 (2007).

[4] K. J. Eskola, H. Paukkunen, and C. A. Salgado, EPS09: A New Generation of NLO and LO Nuclear Parton Distribution Functions, J. High Energy Phys. 04 (2009) 065.

[5] K. Kovařík, I. Schienbein, F. I. Olness, J. Y. Yu, C. Keppel, J. G. Morfín, J. F. Owens, and T. Stavreva, Nuclear Corrections in Neutrino-Nucleus DIS and their Compatibility with Global NPDF Analyses, Phys. Rev. Lett. **106**, 122301 (2011).

[6] D. de Florian, R. Sassot, P. Zurita, and M. Stratmann, Global Analysis of Nuclear Parton Distributions, Phys. Rev. D **85**, 074028 (2012).

[7] I. Helenius, K. J. Eskola, H. Honkanen, and C. A. Salgado, Impact-Parameter Dependent Nuclear Parton Distribution Functions: EPS09s and EKS98s and Their Applications in Nuclear Hard Processes, J. High Energy Phys. 07 (2012) 073.

[8] C. Lourenço, R. Vogt, and Hermine K. Wöhri, Energy dependence of J/ψ absorption in proton-nucleus collisions, J. High Energy Phys. 02 (2009) 014.

[9] R. Arnaldi *et al.* (NA60 Collaboration), J/ψ production in proton-nucleus collisions at 158 and 400 GeV, Phys. Lett. B **706**, 263 (2012).

[10] D. C. McGlinchey, A. D. Frawley, and R. Vogt, Impact parameter dependence of the nuclear modification of J/ψ production in d + Au collisions at $\sqrt{S_{NN}} = 200$ GeV, Phys. Rev. C **87**, 054910 (2013).

[11] F. Arleo and S. Peigne, J/ψ Suppression in p-A Collisions from Parton Energy Loss in Cold QCD Matter, Phys. Rev. Lett. **109**, 122301 (2012).

[12] X. Zhao and R. Rapp, Charmonium in Medium: From Correlators to Experiment, Phys. Rev. C **82**, 064905 (2010).

[13] B. Alessandro *et al.* (NA50 Collaboration), A New measurement of J/psi suppression in Pb-Pb collisions at 158 GeV per nucleon, Eur. Phys. J. C **39**, 335 (2005).

[14] A. Adare *et al.* (PHENIX Collaboration), J/ψ suppression at forward rapidity in Au+Au collisions at $\sqrt{s_{NN}} = 39$ and 62. 4 GeV, Phys. Rev. C **86**, 064901 (2012).

[15] W. Zha (STAR Collaboration), Recent measurements of quarkonium production in $p + p$ and $A + A$ collisions from the STAR experiment, Nucl. Phys. A **931**, 596 (2014).

[16] A. Adare *et al.* (PHENIX Collaboration), J/ψ suppression at forward rapidity in Au+Au collisions at $\sqrt{s_{NN}} = 200$ GeV, Phys. Rev. C **84**, 054912 (2011).

[17] A. Adare *et al.*, J/ψ Production vs Centrality, Transverse Momentum, and Rapidity in Au+Au Collisions at $\sqrt{s_{NN}} = 200$ GeV, Phys. Rev. Lett. **98**, 232301 (2007).

[18] L. Adamczyk *et al.* (STAR Collaboration), J/ψ production at low p_T in Au+Au and Cu+Cu collisions at $\sqrt{s_{NN}} = 200$ GeV with the STAR detector, Phys. Rev. C **90**, 024906 (2014).

[19] B. B. Abelev *et al.* (ALICE Collaboration), Centrality, rapidity and transverse momentum dependence of J/ψ suppression in Pb-Pb collisions at $\sqrt{s_{NN}} = 2.76$ TeV, Phys. Lett. B **734**, 314 (2014).

[20] J. Adam *et al.* (ALICE Collaboration), Differential studies of inclusive J/ψ and ψ(2S) production at forward rapidity in Pb-Pb collisions at $\sqrt{s_{\rm NN}} = 2.76$ TeV, arXiv:1506.08804 (2015).

[21] K. Zhou, N. Xu, Z. Xu, and P. Zhuang, Medium effects on charmonium production at ultrarelativistic energies available at the CERN Large Hadron Collider, Phys. Rev. C **89**, 054911 (2014).

[22] D. Kikola, G. Odyniec, and R. Vogt, Prospects for quarkonia production studies in U + U collisions, Phys. Rev. C **84**, 054907 (2011).

[23] K. Adcox *et al.* (PHENIX Collaboration), PHENIX detector overview, Nucl. Instrum. Methods Phys. Res., Sec. A **499**, 469 (2003).

[24] H. Akikawa *et al.* (PHENIX Collaboration), PHENIX muon arms, Nucl. Instrum. Methods Phys. Res., Sec. A **499**, 537 (2003).

[25] S. Aronson *et al.* (PHENIX Collaboration), The PHENIX Detector, Nucl. Instrum. Methods Phys. Res., Sec. A **499**, 480 (2003).

[26] M. L. Miller, K. Reygers, S. J. Sanders, and P. Steinberg, Glauber modeling in high energy nuclear collisions, Ann. Rev. Nucl. Part. Sci. **57**, 205 (2007).

[27] H. Masui, B. Mohanty, and N. Xu, Predictions of elliptic flow and nuclear modification factor from 200 GeV U + U collisions at RHIC, Phys. Lett. B **679**, 440 (2009).

[28] Q. Y. Shou, Y. G. Ma, P. Sorensen, A. H. Tang, F. Videbaek, and H. Wang, Parameterization of Deformed Nuclei for Glauber Modeling in Relativistic Heavy Ion Collisions, Phys. Lett. B **749**, 215 (2015).

[29] W. T. Milner, C. E. Bemis, and F. K. McGowan, Quadrupole and hexadecapole deformations in the actinide nuclei, Phys. Rev. C **16**, 1686 (1977).

[30] A. Adare *et al.* (PHENIX Collaboration), Ground and excited charmonium state production in $p + p$ collisions at $\sqrt{s} = 200$ GeV, Phys. Rev. D **85**, 092004 (2012).

[31] C. Aidala *et al.* (PHENIX Collaboration), Nuclear matter effects on J/ψ production in asymmetric Cu+Au collisions at $\sqrt{s_{NN}} = 200$ GeV, Phys. Rev. C **90**, 064908 (2014).

[32] R. Brun, F. Carminati, and S. Giani, GEANT Detector Description and Simulation Tool, CERN-W5013 (1994).

[33] T. Sjöstrand, S Mrenna, and P Skands, PYTHIA 6. 4 physics and manual, J. High Energy Phys. 05 (2006) 026.

[34] A. Adare *et al.* (PHENIX Collaboration), Cold Nuclear Matter Effects on J/ψ Yields as a Function of Rapidity and Nuclear Geometry in Deuteron-Gold Collisions at $\sqrt{s_{NN}} = 200$ GeV, Phys. Rev. Lett. **107**, 142301 (2011).

[35] A. Adare *et al.* (PHENIX Collaboration), J/ψ Production in $\sqrt{s_{NN}} = 200$ GeV Cu+Cu Collisions, Phys. Rev. Lett. **101**, 122301 (2008).